3rd URSI AT-AP-RASC, Gran Canaria, 29 May – 3 June 2022

Analysis on the accuracy of the Embedded Element Patterns for one station of SKA-Low by using a Radius of Influence approach

Mirko Bercigli[(1)], Pietro Bolli*[(2)], and Paola Di Ninni [(2)]
(1) Ingegneria dei Sistemi, Pisa, Italy
(2) INAF, Arcetri Astrophysical Observatory, Florence, Italy

Abstract

This paper provides a detailed analysis on the use of a radius of influence approach to reduce the computational time for analyzing the EM performance of the radio telescope SKA-Low. For one station of SKA-Low, composed by 256 log-periodic antennas, we evaluate the accuracy in the individual antenna patterns and the duration of the EM simulations applying different radii of influence with respect to the full station case.

1. Introduction

The radio astronomical community is involved in the construction of the most sensitive radio telescope ever built: the Square Kilometer Array (SKA, https://www.skatelescope.org/). This will consist of two radio telescopes observing different windows of the radio spectrum. The low-frequency instrument (SKA-Low) operating between 50 and 350 MHz is going to be built in Western Australia. It will be an interferometer composed by 512 stations, each of them formed by 256 dual-polarized log-periodic dipole antennas (SKALA4.1, [1]) quasi-randomly distributed over a circular patch with around 40-m diameter.

High-fidelity computational electromagnetic (CEM) analysis is vital for the success of this major effort. Recently, the EM performance of the prototype station Aperture Array Verification System version 2 (AAVS2, [2]) deployed at the Murchison Radio-astronomy Observatory have been predicted by CEM techniques [3]. This analysis turns out to be very important to estimate the performance of the array, including mutual coupling effects, and to define possible calibration strategies to account for the different antenna responses, the so-called Embedded Element Patterns (EEPs).

The analysis conducted in [3] is based on accelerated techniques available in commercial EM software. In particular, the Multi-Level Fast-Multipole Algorithm (MLFMA) was used for the iterative solution of the Method of Moment (MoM) for AAVS2 with typical run-times on a multicore workstation ranging from several hours to many days per frequency point.

Different accelerated techniques to speed up the EM simulations have been proposed, such as in [4] where a macro basis function approach and an interpolatory technique have been presented and applied to SKA-Low. Moreover, in [5] the authors propose a combination of spherical wave to represent EEPs and a study on the impact of the Radius of Influence (RoI) on the error of the array beam pattern.

In this paper, we apply a RoI technique to AAVS2 to assess the accuracy in computing the EEPs with respect to a full station approach. This assessment is conducted using as a figure of merit the Envelope Correlation Coefficient (ECC). Finally, we verify the reduction in the model complexity (as degrees of freedom) and in the running time thanks to this simplified approach.

2. Radius of Influence approach in Galileo solver

The proposed method is applied by using a full-wave MoM-based solver, the IDS Method of Moment Multi-Port (IDSMMMP) numerical code available in the Galileo suite (https://www.idscorporation.com/pf/galileo-suite/). This code manages geometries discretized through triangles and wires and it models the EM problem through the Electric Field Integral Equation/Mixed Potentials approach. In addition to the standard features, IDSMMMP also includes the MLFMA fast method [6] that uses a set of preconditioners to speed-up the iterative solution.

The conventional way to numerically analyze the AAVS2 station is to solve a single EM problem composed by 256 antennas. This approach is here referred as Full Station (FS) solution and is considered the most rigorous analysis as it takes into account all possible interaction among the antennas of the array, including antennas located on opposite sides of the station. On the other hand, the RoI approach consists in solving a different EM problem for every single antenna of the array (identified as antenna pivot). For each antenna pivot, the geometry of the model is different and consists of a limited number of antennas whose separation from the antenna pivot is below a certain distance (RoI). Antennas located at larger distances from the antenna pivot are therefore neglected by the EM analysis. This implies that the lower the radius of influence,

the faster the computational time at the cost of a lower accuracy of the EEP with respect to the FS case.

The flow chart depicted in Fig. 1 shows the algorithm to solve the EM problem by using a MLFMA approach. The algorithm consists of two main phases. The first one, independent by the excitation, calculates the matrices necessary for the MLFMA factorization of the linear system describing the problem ($Z = Z_{\text{near}} + Z_{\text{far}}$) and the preconditioner. In the second phase the problem is solved for each excitation (i.e. antenna port) through an iterative method. This algorithm is valid for the FS case, where the impedance matrix (Z) is given by the model composed of 256 antennas and $N_p = 512$ (2 ports multiplied by 256 antennas). For the RoI approach, the algorithm is still the same but with a Z matrix (and preconditioner) reduced in dimension due to the smaller number of antennas and $N_p = 2$ (2 ports of the antenna pivot). However, in the latter case, the problem must be repeated 256 times, one for each antenna pivot.

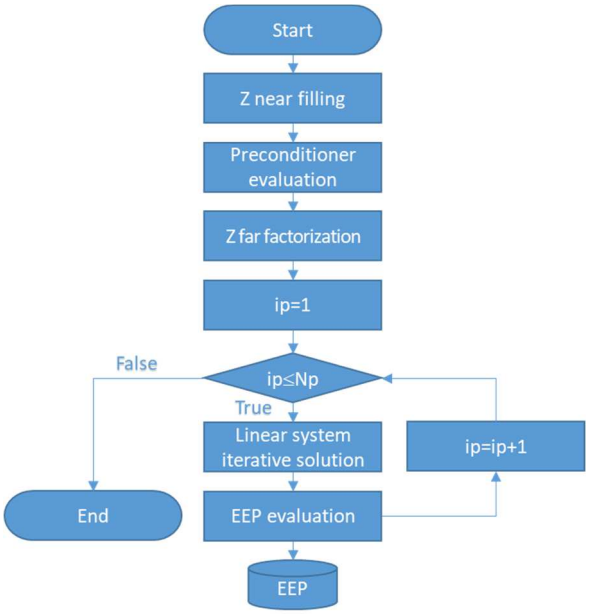

Figure 1. Flow-chart of the Galileo solver implementing the MLFMA method. This algorithm is in principle valid both for the FS case and for the RoI approach, but for the RoI approach the dimension of Z matrix and $\boldsymbol{N_p}$ are lower than for the FS.

3. Simulations and Data Analysis

The 256 SKALA4.1 antennas of AAVS2 are deployed in a quasi-random fashion as depicted in Fig. 2 and laid over a metallic ground plane, which is modelled as an infinite plane of perfect electrical conductor.

The three antennas highlighted in Fig. 2 are those selected to carry out this study. Two of them are located close to the center of the station, while the other one is located approximately in the middle of the radius of the station. Seven circles characterized by a different radius (RoI) and centered in the outer antenna (#60) are drawn in Fig. 2.

Depending on the antenna position, for the same RoI the number of passive antennas can vary significantly. For the selected antennas, Table 1 summarizes the values of RoIs used in this analysis and the number of antennas inside each circle. Moreover, Table 1 gives, for each RoI, the number of passive antennas averaged for all antenna pivots together with their standard deviation.

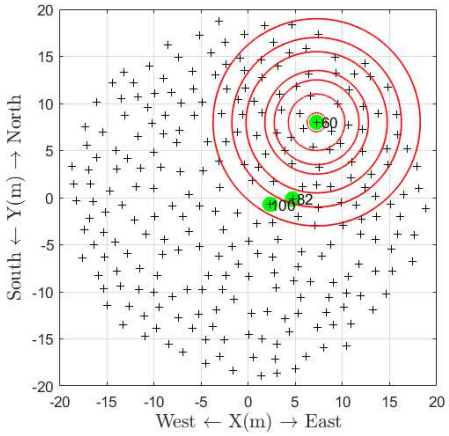

Figure 2. AAVS2.0 layout with the three selected antennas (#60, #82, #100) indicated with a green full-dot and the seven circles (in red) centered in antenna #60 and computed with the different RoIs.

Table 3. Number of passive antennas for different radii of influence and for three antenna pivots. The last two rows indicate the average in the number of antennas considering, as antenna pivot, all antennas of AAVS2 and its standard deviation.

	Radius of influence expressed in meter						
	1*	3	4.5	5.5	7.5	9	11
#60	0	6	14	21	37	58	74
#82	0	5	11	17	35	54	78
#100	0	4	11	18	33	52	78
Ave.	0	5.0	11.7	17.4	31.3	43.4	61.5
Std	0	1.3	2.6	3.7	6.6	9.7	14.4

* The case of radius equal to 1 m corresponds to the isolated antenna.

For the polarization aligned to the Y-axis (North-South in Fig. 2) of antenna #60, Fig. 3 shows the directivities in the E-plane at 50 and 350 MHz. The directivities are computed for seven cases associated to different RoIs. As a reference, the directivity computed for the FS case is also plotted. For the two extreme cases, antenna isolated (ISO) and FS, the patterns are indicated with blue and black dashed-lines, respectively. The bottom sub-plots of Fig. 3 show the normalized differences of the patterns computed with RoIs with respect to the FS case. At 50 MHz, where the mutual coupling effect is stronger, a significant difference between the patterns can be noticed both in the main beam and at the horizon. The maximum normalized difference range from ≥ ~20% (for RoI ≤ 5.5 m) to ~5% (for RoI ≥ 7.5 m). Interestingly, the maximum difference does not decrease when the RoI increases from 7.5 to 11 m, likely due the fact that the antennas mostly coupled to antenna #60 are already included in the RoI=7.5 m case. At 350 MHz the effect of the mutual coupling is less pronounced. However, for RoI ≤ 5.5 m the maximum difference is always ~20%, while

this decreases to 7.7% and 6.5% at RoI=9 and 11 m respectively.

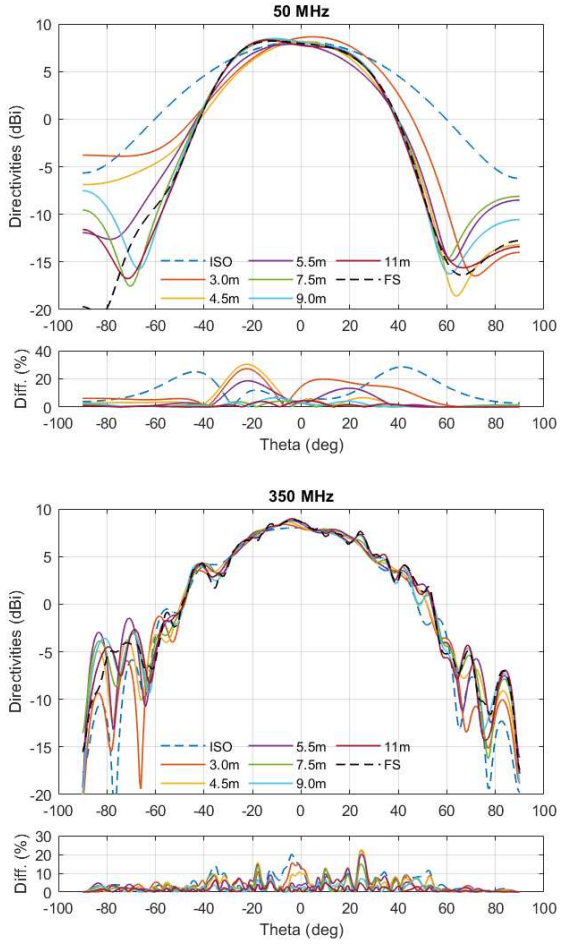

Figure 3. Directivities of antenna #60 at 50 and 350 MHz for the isolated case (blue dashed-line), the FS case (black dashed-line), and all the investigated RoIs (colored continuous-line). The lower sub-plots show the normalized difference (%) between directivities computed with RoIs and the FS case.

To get rid of the angular dependence of the patterns, the overall accuracy of the EEPs is examined by using the Envelope Correlation Coefficient (ECC) [7]. This parameter provides a cumulative way to define the differences between the EEPs computed with the RoI approach and with the FS case. For antenna #*i*, the ECC is given by the following integral extended to the hemisphere above the horizon:

$$ECC_i = \frac{\left|\iint\left[\vec{E}_i^{RoI}(\theta,\varphi)\cdot\vec{E}_i^{FS}(\theta,\varphi)\right]d\Omega\right|^2}{\iint\left|\vec{E}_i^{RoI}(\theta,\varphi)\right|^2 d\Omega \iint\left|\vec{E}_i^{FS}(\theta,\varphi)\right|^2 d\Omega}$$

where $\vec{E}_i^{RoI}(\theta,\varphi)$ is the complex far-field radiation pattern of the antenna #*i* computed for a specific RoI, $\vec{E}_i^{FS}(\theta,\varphi)$ is the complex far-field radiation pattern for the FS case of the same antenna and · denotes the Hermitian product.

Fig. 4 shows the ECC trends as a function of the RoI for the three antennas (both polarizations) at 50 and 350 MHz.

As expected, at both frequencies, the ECCs tend to 1 (corresponding to $\vec{E}_i^{RoI}(\theta,\varphi) = \vec{E}_i^{FS}(\theta,\varphi)$) when the RoI grows. Focusing on 50 MHz, we can see that the ECCs can be as low as ~0.5 reflecting large discrepancies in the patterns obtained with small RoIs with respect to the FS case. On the other hand, at 350 MHz, the ECCs vary between ~0.9 and ~0.98, which means that also for small RoIs the EEPs are quite accurate as the mutual coupling with antennas excluded by the analysis is low.

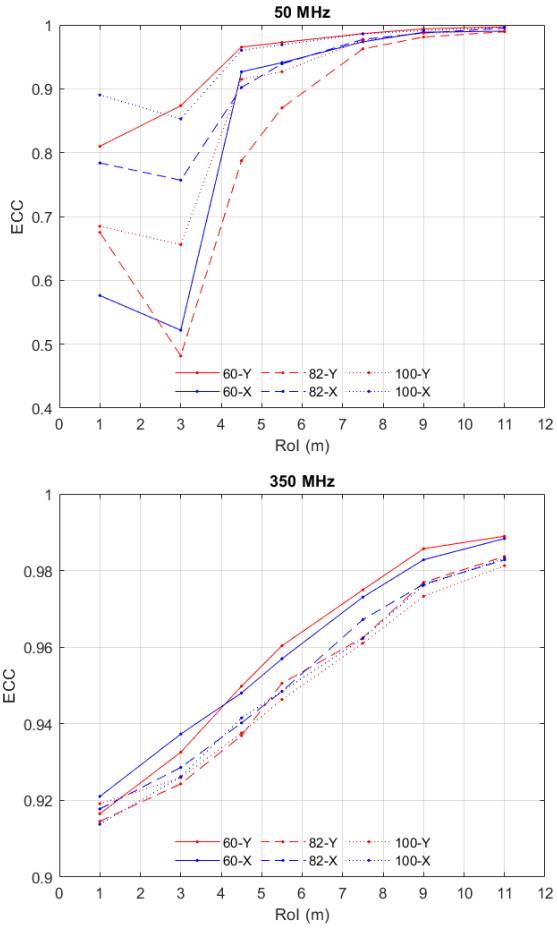

Figure 4. ECCs at 50 and 350 MHz for antenna #60 (continuous-line), #82 (dashed-line), #100 (dotted-line). Red and blue colours refer to Y- and X-polarization, respectively.

Fig. 4 also shows that, especially at 50 MHz and for smaller RoIs, each antenna/polarization provides a quite different ECC value. This depends on the local position of the antenna in the array and consequently on the distribution of the surrounding antennas. In order to remove this antenna dependence, we average the ECC values among the three antennas and the two polarizations. This is summarized by the four curves (each of them associated to a different frequency) in Fig. 5. The curves show that above 110 MHz, the ISO cases (RoI=1m) provide on average a difference to the FS case less than 10%, while for RoI $\geq$ 9 m this decreases to 2.5%. On the other hand, at 50 MHz, where the array is dense, small RoIs determine very inaccurate results; while for RoI > 7.5 m the differences to the FS case are less than 2.5%.

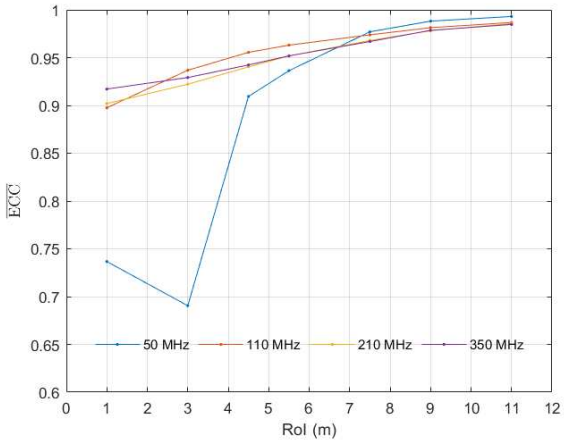

Figure 5. Averaged ECCs at 50, 110, 210 and 350 MHz for different RoIs.

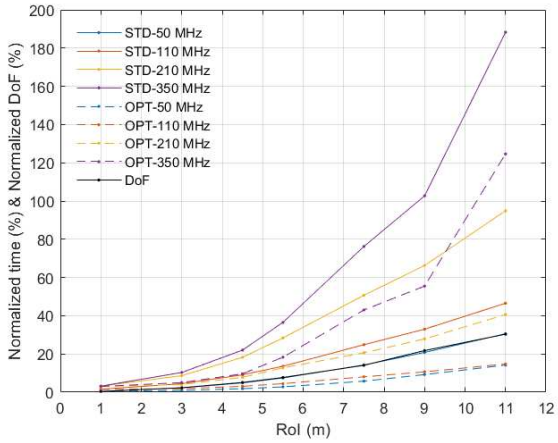

Figure 6. Percentage value of the DoF normalized to the DoF of the FS model as a function of the RoI (black curve). The coloured curves give the percentage saving in the normalized running time at different frequencies with respect to the FS case. Dashed and continuos curves refer to the current algorithm and to an optimized version, respectively.

As a final step, we analyze the reduction of degrees of freedom (DoF) and of running time for the simplified RoI approach. DoF are here defined as the sum of the basic function of Rao-Wilton-Glisson on triangles, Piecewise-Linear on wires and attachment between triangles and wires in the EM model. The black curve in Fig. 6 shows the DoF averaged over the three antenna pivots and normalized to the DoF of the FS model. The FS model involves around 2.2E6 DoFs, while the isolated case only 8.8E3 DoF (0.4%). At RoI=7.5 m the DoF of the EM model is ~15% that of the FS model and then it reaches 30% at RoI=11 m. This is reflected in the duration of the EM analysis to compute all EEPs. The coloured-continuous curves in Fig. 6 refer to the running time by applying the algorithm as described in Fig. 1 for the RoIs approach normalized to the FS case. The time saving is frequency dependent and more pronounced at lower frequency (at 50 MHz the computation time for RoI=11 m is 30% of the FS case). On the other hand, for the same RoI at 350 MHz, the FS analysis is still more convenient than the RoI approach due to some redundancies in the latter computation. However, by optimizing the calculation of the Z_{near} matrix (see Fig. 1) the running time can be halved with respect to the current RoI algorithm (see coloured-dashed curves).

Finally, by exploiting the fact that the simulations for each antenna pivot are independent each other, an additional remarkable time reduction (not shown here), which would bring this approach definitively more convenient than the FS case also at 350 MHz, would be given by the parallelization of the algorithm.

4. Conclusion

At the current stage, the accuracy required by scientists to model the antenna patterns is not yet fully defined. This depends on the calibration strategy and on the scientific cases. However, this paper shows that a significant amount of computational time and complexity can be saved in the EM simulations by using the RoI approach, with a limited reduction in the accuracy of the patterns.

References

[1] P. Bolli, et al., “Test-Driven Design of an Active Dual-Polarized Log-Periodic Antenna for the Square Kilometre Array,” *IEEE Open Journal of Antennas and Propagation*, **1**, pp. 253-263, 2020.

[2] A.J.J. van Es, et al., “A prototype model for evaluating SKA-LOW station calibration,” *Ground-based and Airborne Telescopes VIII, Proceedings of SPIE*, **11445**, (online), 14 – 18 December, 2020.

[3] P. Bolli, D. B. Davidson, M. Bercigli, P. Di Ninni, M. G. Labate, D. Ung, G. Virone, “Computational electromagnetics for the SKA-Low prototype station AAVS2”, *Journal of Astronomical Telescopes, Instruments, and Systems*, **8**, 1, 011017, 2022.

[4] H. Bui-Van, et al., "Fast and Accurate Simulation Technique for Large Irregular Arrays," *IEEE Transactions on Antennas and Propagation*, **66**, 4, pp. 1805-1817, April 2018.

[5] E. de Lera Acedo, N. Razavi-Ghods, D. G. Ovejéro, R. Sarkis and C. Craeye, "Compact representation of the effects of mutual coupling in non-regular arrays devoted to the SKA telescope," *International Conference on Electromagnetics in Advanced Applications*, 2011, pp. 390-393.

[6] W. C. Chew, J.-M. Jin, E. Michielssen, and J. Song, ed., Fast and Efficient Algorithms in Computational Electromagnetics, Boston: Artech House, 2001.

[7] S. Blanch, J. Romeu, and D. I. Corbella, “Exact presentation of antenna system diversity performance from input parameter description,” *Electronics Letters*, **39**, 9, pp. 705-707, June 2003.